



# Microstructure and Mechanical Properties of a Multiphase FeCrCuMnNi High-Entropy Alloy

Ali Shabani, Mohammad Reza Toroghinejad, Ali Shafyei, and Roland E. Logé

(Submitted September 24, 2017; in revised form January 20, 2019; published online April 8, 2019)

A FeCrCuMnNi high-entropy alloy was produced using vacuum induction melting, starting from high-purity raw materials. The microstructure and mechanical properties of the as-cast FeCrCuMnNi alloy were studied, considering x-ray diffraction (XRD), scanning electron microscopy, and hardness and tensile tests. XRD results revealed the existence of two FCC phases and one BCC phase. Microstructural evaluation illustrated that the as-cast alloy has a typical cast dendritic structure, where dendrite regions (BCC) were enriched in Cr and Fe. Interdendritic regions were saturated with Cu and Ni and revealed G/B(T)  $\{110\} \langle 111 \rangle$  and Brass  $\{110\} \langle 112 \rangle$  as the major texture components. The produced alloy revealed an excellent compromise in mechanical properties due to the mixture of solid solution phases with different structures: 300 HV hardness, 950 MPa ultimate tensile strength and 14% elongation. Microhardness test results also revealed that the BCC phase was the hardest phase. The fracture surface evidenced a typical ductile failure. Furthermore, heat treatment results revealed that phase composition remained stable after annealing up to 650 °C. Phase transformation occurred at higher temperatures in order to form more stable phases; therefore, FCC2 phase grew at the expense of the BCC phase.

**Keywords** FeCrCuMnNi high-entropy alloy, heat treatment, mechanical properties, microstructure, SEM

## 1. Introduction

High-entropy alloys (HEAs) are equiatomic or near-equiatomic metallic solid solutions composed of 5 to 13 major elements, and the molar ratio of each element varies from 5 to 35 at.% (Ref 1, 2). HEAs usually show very simple structures such as face-centered cubic (FCC) and/or body-centered cubic (BCC) solid solutions instead of complex intermetallics. This is often attributed to their high configurational entropy (Ref 3, 4).

In the past few years, a large numbers of studies have been conducted on the microstructure and mechanical properties of different HEAs (Ref 5-9). The researches on mechanical properties were mainly restricted to the mechanical properties of the as-cast single-phase alloys (Ref 10-13). Shun and Du (Ref 11) reported a medium-range strength ( $\sim 350$  MPa UTS) and good ductility ( $\sim 60\%$  elongation) for an as-cast  $\text{Al}_{0.3}\text{CoCrFeNi}$  HEA with single FCC phase. He et al. (Ref 12) reported that by moving toward a single BCC phase HEA from a FCC one, the strength increases but the ductility

decreases remarkably. Generally, single-phase FCC-type HEAs exhibit high ductility and medium to high tensile strength. In contrast, BCC-type HEAs have high strength, typically associated with low ductility (Ref 1, 13). Basically, single-phased HEAs have been found to reach a reasonable balance between strength and (tensile) ductility with difficulty (Ref 14). Therefore, a mixture of these phases could lead to an interesting compromise between hardness and ductility. Recently, a few researches have been conducted with the aim to optimize the mechanical properties of dual-phase HEAs (Ref 5-7, 14, 15). It seems that this combination can lead to both high fracture strength and high ductility as reported in different researches (Ref 7, 14).

FeCrCuMnNi was first reported as a new HEA consisting of the mixture of FCC and BCC phases by Li et al. (Ref 16). However, the microstructure and mechanical properties of this alloy were not sufficiently investigated (Ref 15, 16). Therefore, the aim of this research was to perform such an investigation through looking at the structure, microstructure and mechanical properties of the as-cast equiatomic FeCrCuMnNi high-entropy alloy. The alloy was produced using a vacuum induction melting furnace. The formation of solid solution phases was evaluated through x-ray diffraction (XRD) and thermodynamic calculations. Grain structures and chemical compositions were assessed through electron backscatter diffraction/energy-dispersive x-ray spectroscopy (EBSD/EDS) together with tensile, hardness and microhardness tests.

## 2. Experimental Procedure

The FeCrCuMnNi high-entropy alloy was produced through vacuum induction melting of high-purity (more than 99.85%) raw materials. Before charging the raw materials into the crucible, all alloying elements were cleaned with acetone and dried. Subsequently, the chamber was brought to a vacuum of

Ali Shabani, Department of Materials Engineering, Isfahan University of Technology, Isfahan 84156-83111, Iran; and Thermomechanical Metallurgy Laboratory - PX Group Chair, Ecole Polytechnique Fédérale de Lausanne (EPFL), 2002 Neuchâtel, Switzerland; Mohammad Reza Toroghinejad and Ali Shafyei, Department of Materials Engineering, Isfahan University of Technology, Isfahan 84156-83111, Iran; and Roland E. Logé, Thermomechanical Metallurgy Laboratory - PX Group Chair, Ecole Polytechnique Fédérale de Lausanne (EPFL), 2002 Neuchâtel, Switzerland. Contact e-mails: ali.shabani@ma.iut.ac.ir, toroghi@cc.iut.ac.ir, shafyei@cc.iut.ac.ir, and roland.loge@epfl.ch.

$1 \times 10^{-3}$  Pa and then filled with high-purity argon to 1 atm. The vacuum-filling cycle was repeated two times. The alloy was then casted into a graphite mold with dimensions of  $15 \times 100 \times 100$  mm. To ensure compositional homogeneity, the ingots were remelted two times. In order to study the effects of different heat treatment temperatures, specimens with dimensions of  $100 \text{ mm} \times 10 \text{ mm} \times 1 \text{ mm}$  were cut from the as-cast ingot and heat-treated at different temperatures (500 °C, 600 °C, 650 °C, 700 °C, 750 °C, 800 °C, 900 °C and 1000 °C) for 4 h in a vacuum furnace.

The crystal structure was investigated using a Philips x-ray diffractometer with Cu Ka ( $\lambda = 0.15406$  nm) diffraction generated at 40 kV and 30 mA with the scanning angles ranging from 20 to 100 degrees and a step size of  $0.05^\circ$ . The microstructure and texture of the as-solidified sample were analyzed using a scanning electron microscope (SEM) (Philips FEI XLF30) equipped with backscatter electron (BSE) and EBSD detectors.

Tensile test samples were machined from the as-cast ingot through electrical discharge machining (EDM). The gauge width and length were 2.5 and 6.4 mm, respectively. The tensile tests were performed using a Hounsfield H25KS testing machine. The Vickers hardness test was also performed on the sample under a load of 10 kg, during 30 s. For each sample 8 tests were performed, from the results of which the maximum and minimum values were removed. In some tests, a lower load of 5 g (during 10 s) was used in order to investigate the hardness of individual phases of the alloy.

### 3. Results and Discussion

#### 3.1 Structural Characterization

The XRD pattern of the FeCrCuMnNi high-entropy alloy is shown in Fig. 1, indicating two FCC phases and one BCC phase. Generally, Cu and Ni are FCC-forming elements and the presence of Cr and Fe elements in the structure leads to the formation of FCC + BCC mixed structures (Ref 15, 17). Therefore, the structure of the produced alloy includes a mixture of FCC and BCC phases. The lattice constants of the

FCC (1 and 2) and BCC solid solutions were calculated from the principal peaks to be 3.671, 3.613 and 2.876 Å, respectively.

High-entropy alloys are usually identified as alloys with a disordered solid solution phase structure. In general, these alloys contain 5 to 13 elements in an equiatomic or a near-equiatomic concentration, with high configurational entropy (Ref 1, 18). In order to predict structural stability and solid solution phase formation in HEAs, several physical parameters have been proposed. These parameters were calculated using the following equations (Ref 1, 19).

$$\Delta S_{\text{mix}} = -R \sum_{i=1}^n X_i \ln X_i \quad (\text{Eq 1})$$

$$\Delta H_{\text{mix}} = \sum_{i=1, j \neq i}^n 4\Delta H_{AB}^{\text{mix}} X_i X_j \quad (\text{Eq 2})$$

$$T_m = \sum_{i=1}^n X_i (T_m)_i \quad (\text{Eq 3})$$

$$\delta = \sqrt{\sum_{i=1}^N X_i \left( 1 - r_i / \left( \sum_{i=1}^N X_i r_i \right) \right)^2} \quad (\text{Eq 4})$$

$$\Omega = \frac{T_m \Delta S_{\text{mix}}}{|\Delta H_{\text{mix}}|} \quad (\text{Eq 5})$$

where  $\Delta S_{\text{mix}}$  is the entropy of mixing,  $X_i$  is the mole percent of component  $i$ ,  $R$  is the gas constant,  $\Delta H_{\text{mix}}$  is the enthalpy of mixing,  $\Delta H_{AB}^{\text{mix}}$  is the enthalpy of mixing of binary liquid alloys, and  $(T_m)_i$  is the melting point of component  $i$  and  $r_i$  is its atomic radius. The calculated values of these parameters are presented in Table 1.  $\Omega$  and  $\delta$  are two parameters widely used to predict the phase formation in multi-principal component alloys (Ref 2, 19, 20).  $\delta$  is the atomic size difference, and  $\Omega$  is the combined effects of the mixing entropy, mixing enthalpy and melting temperature. In order to form solid solution in a multi-principal component alloy,  $\Omega \geq 1.1$  and  $\delta \leq 6.6\%$  are required (Ref

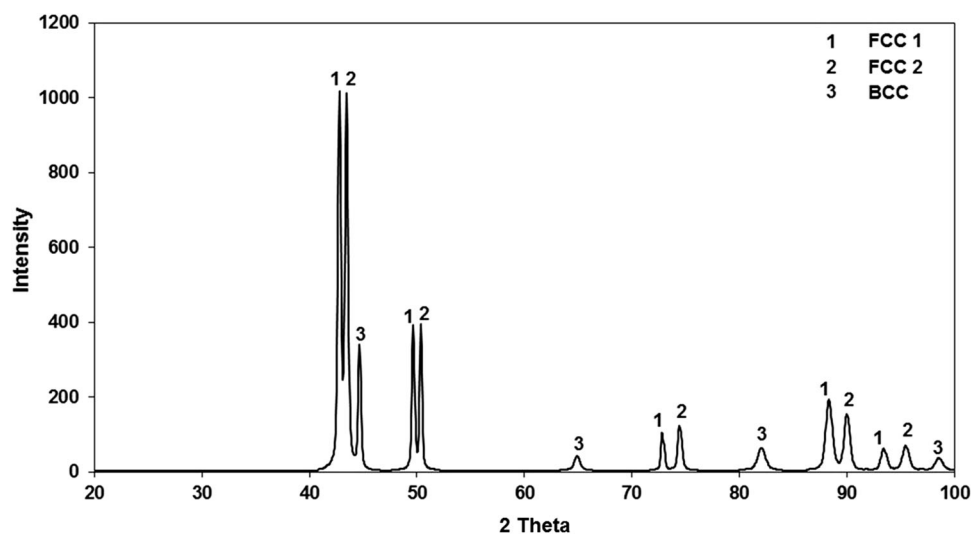


Fig. 1 XRD pattern of as-cast FeCrCuMnNi high-entropy alloy

19, 21), which is the case here. In addition, Senkov and Miracle proposed a new thermodynamic parameter to predict the formation of solid solution in HEAs (Ref 22). They reported that solid solution forms in HEAs when  $K_3 > K_1$ . These parameters were defined as follows:

$$\Delta H_{\text{IM}} = \sum_{i < j} 4H_{ij}^{\text{IM}} X_i X_j \quad (\text{Eq 6})$$

$$K_1 = \frac{\Delta H_{\text{IM}}}{\Delta H_{\text{mix}}} \quad (\text{Eq 7})$$

$$K_2 = \frac{\Delta S_{\text{IM}}}{\Delta S_{\text{mix}}} \quad (\text{Eq 8})$$

$$K_3 = \frac{T \Delta S_{\text{mix}}}{|\Delta H_{\text{mix}}|} (1 - K_2) + 1 \quad (\text{Eq 9})$$

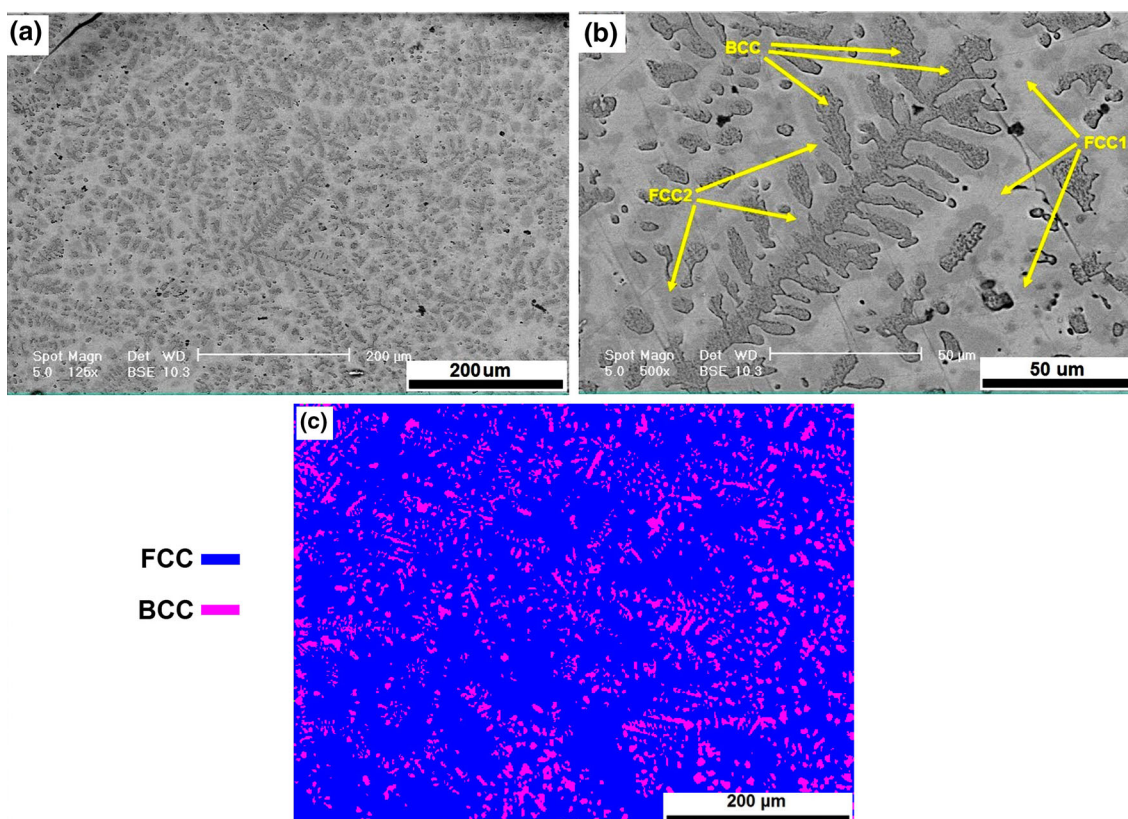
where  $\Delta H_{\text{IM}}$  and  $\Delta S_{\text{IM}}$  are the enthalpy and the entropy of formation of ordered binary compounds. As shown in Table 1, the values of  $K_1$  and  $K_3$  for the FeCrCuMnNi alloy meet the criterion of the formation of the solid solution phase.

Figure 2(a) and (b) illustrates the typical cast dendritic structure of the FeCrCuMnNi high-entropy alloy. In Fig. 2(b), three different phases can be distinguished, which is consistent with XRD results. Furthermore, the phase map of the as-cast sample extracted from EBSD is shown in Fig. 2(c). It can be seen that FCC phases were indexed as interdendritic regions (IDRs) and the BCC phase was indexed as dendrite regions (DRs). However, in IDRs, two FCC phases were not distinguished by EBSD due to their similar lattice parameter. This figure also reveals that the as-cast sample contains almost 82% and 18% of the FCC and BCC phases, respectively.

In order to characterize the compositions of the individual phases, at least 10 EDS points were conducted on each phase. The specification and the chemical composition (in at.%) of the three phases characterized by EDS and XRD are shown in Table 2. As shown in this table, DRs have a BCC structure saturated with Cr ( $\sim 38$  at.%) and Fe ( $\sim 31$  at.%). This phase can be seen as the darkest phase in Fig. 2(b), since Cr is the lightest element in the alloy composition. IDRs consist of two FCC phases. The main phase (FCC1) is enriched in Cu ( $\sim 45$  at.%). This phase can be distinguished as the brightest phase, since Cu is the heaviest element in the alloy. Moreover,

**Table 1** Calculated parameters of  $\Delta S_{\text{mix}}$ ,  $\Delta H_{\text{mix}}$ ,  $T_m$ ,  $\delta$ ,  $\Omega$ ,  $K_1$  and  $K_3$  for the FeCrCuMnNi alloy

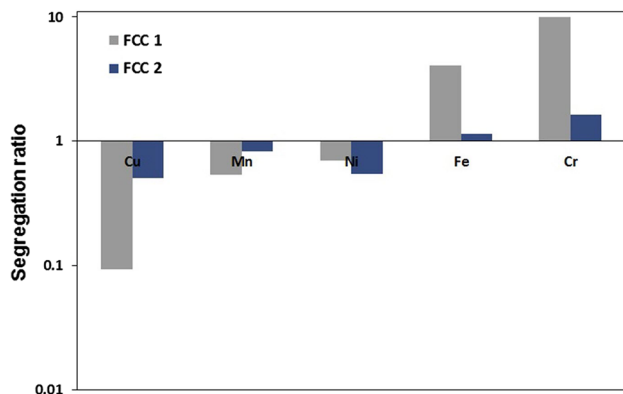
$\Delta S_{\text{mix}}$ , J/K mol <sup>-1</sup>	$\Delta H_{\text{mix}}$ , kJ/mol	$T_m$ , K°	$\delta \times 100$	$\Omega$	$K_1$	$K_3$
13.38	2.72	1720	4.2	8.46	- 0.88	9.4



**Fig. 2** (a) and (b) SEM microstructure of the as-cast FeCrCuMnNi high-entropy alloy at different magnifications and (c) phase map of the as-cast sample

**Table 2** Specification of the as-cast sample and the three phases (at.%) of the FeCrCuMnNi alloy

	Structure	Fe, %	Cr, %	Cu, %	Mn, %	Ni, %	Lattice parameter, Å
As cast	FCC + BCC	20.0 ± 0.9	19.1 ± 1.1	20.8 ± 1.2	19.9 ± 0.5	20.2 ± 0.7	...
Dendrite	BCC	31.1 ± 1.8	38.0 ± 2.4	4.2 ± 0.8	12.6 ± 1	14.1 ± 1.1	2.876
Interdendrite	FCC1	7.6 ± 1	3.8 ± 0.7	45.1 ± 2.3	23.4 ± 1.3	20.1 ± 1.5	3.671
	FCC2	27.0 ± 2.1	23.2 ± 1.9	8.3 ± 1	15.1 ± 0.9	26.4 ± 2	3.611

**Fig. 3** Elemental segregation ratio of the as-cast FeCrCuMnNi alloy

the FCC2 phase which is saturated with Fe, Ni and Cr can be seen as the gray traces around the DRs.

Generally, the segregation of Cu in the IDRs can be explained by positive mixing enthalpies of Cu with Cr and Fe (Ref 23, 24), i.e., Cu concentrates in the IDRs, in zones with reduced Cr (and Fe) content. On the other hand, negative mixing enthalpies between Cu and Ni lead to the association of Ni to Cu in the IDRs (Ref 23). In addition, segregation of each element in the IDRs can be measured through segregation ratio (SR) using the following equation (Ref 25):

$$SR = \frac{\text{at.\% in IDR}}{\text{at.\% in DR}} \quad (\text{Eq 10})$$

Figure 3 shows the SR of the two FCC phases. For SR of less than 1, the IDRs are enriched in the element, and decreasing this ratio illustrates the enhancement of the segregation in the IDRs. Similarly, for SR of more than 1, the DRs are enriched in the element (Ref 25). Therefore, it can be seen that Cu, Mn and Ni segregate in IDRs and DRs which are enriched in Cr and Fe. As previously mentioned, the SR values indicate that Cu has the maximum segregation in FCC1; however, Cr and Fe segregate in the BCC. Lower ratios of segregation are measured in the FCC2 phase, i.e., its composition is closer to that of the BCC phase.

Chemical (EDS) maps of elements are provided in Fig. 4. This figure confirmed that Cu and Ni segregate to IDRs and Cr segregates to DRs. Furthermore, Fe and Mn almost reveal a homogenous distribution in the as-cast alloy. These results are consistent with those presented in Fig. 3.

Figure 5 illustrates a line scan result, moving from an IDR to the center of a DR. The line scan crosses the three different phases of the alloy. Again, FCC1 exhibits the maximum amount of Cu and Ni elements, while the major elements of BCC are Cr and Fe. Element quantities are not stable within one phase. In the FCC2 phase, Cu and Ni elements have their

maximum amount near the interface with FCC1 and their minimum amount near the interface with the BCC phase. An opposite behavior was observed for Cr. One can therefore interpret the FCC2 phase as a “transition phase” in the alloy structure, which contains 10 to 30 at.% of each element. Cr, Ni and Fe are the major elements, ranging between 23 and 27 at.%, which is again intermediate between the compositions of the FCC1 and BCC phases.

$\varphi_2 = 0^\circ$  and  $45^\circ$  sections of the ODF maps for the FCC and BCC phases are represented in Fig. 6. The important texture components for the alloy (which will be discussed later) are shown in Table 3. It can be seen that Goss/Brass(Twin) (G/B(T))  $\{110\} \langle 111 \rangle$  and Brass  $\{110\} \langle 112 \rangle$  are the major texture components of the FCC phase. In addition, the weak components of Goss  $\{110\} \langle 001 \rangle$ , Rotated cube (Rt-C)  $\{100\} \langle 011 \rangle$  and Copper  $\{112\} \langle 111 \rangle$  can be seen in the ODFs. The BCC phase also shows Rt-C and Copper as the main texture components. To our knowledge no investigation has been conducted on the texture of as-cast HEA; however, surprisingly, Sathiaraj et al. (Ref 26) reported that the texture components of FCC phase are almost the same as cold-rolled and annealed FCC structure HEA. They also reported that the formation of these components is based on the cold-rolled structure, texture and grain size and also depends on the annealing temperature; however, the nature of this texture variation is relatively unexplored (Ref 26-28). In addition, almost the same components were seen in the low SFE FCC/L1<sub>2</sub> phases AlCoCrFe-Ni<sub>2.1</sub> HEA (Ref 29). As FeCrCuMnNi alloy was investigated in as-cast condition, the effect of the previous condition was not meaningful here. Therefore, the authors suggest that the low speed of solidification and the presence of the alloy at high temperatures for a long time may have led to the formation of these components. Additionally, no crystallographic orientation relationship was observed between these two regions (DRs and IDRs).

### 3.2 Mechanical Properties

Figure 7 shows the engineering stress–strain curve of FeCrCuMnNi high-entropy alloy under tension at room temperature. Balanced mechanical properties, i.e., high strength and good ductility, are apparent in this figure. Ultimate tensile strength (UTS), yield strength and elongation are 950 MPa, 615 MPa and 14%, respectively, which are excellent in comparison with other HEAs with as-cast structure (Ref 11, 13). Table 4 reveals the tensile properties of different HEAs for better comparison. The fracture strength of FeCrCuMnNi HEA is much higher than that of most reported FCC HEAs, while at the same time the ductility of this HEA is much higher than most reported BCC HEAs. About 950 MPa UTS and 14.4% elongation with hardness of higher than 300 VHN place the alloy in the category of metals with an excellent combination of mechanical properties.

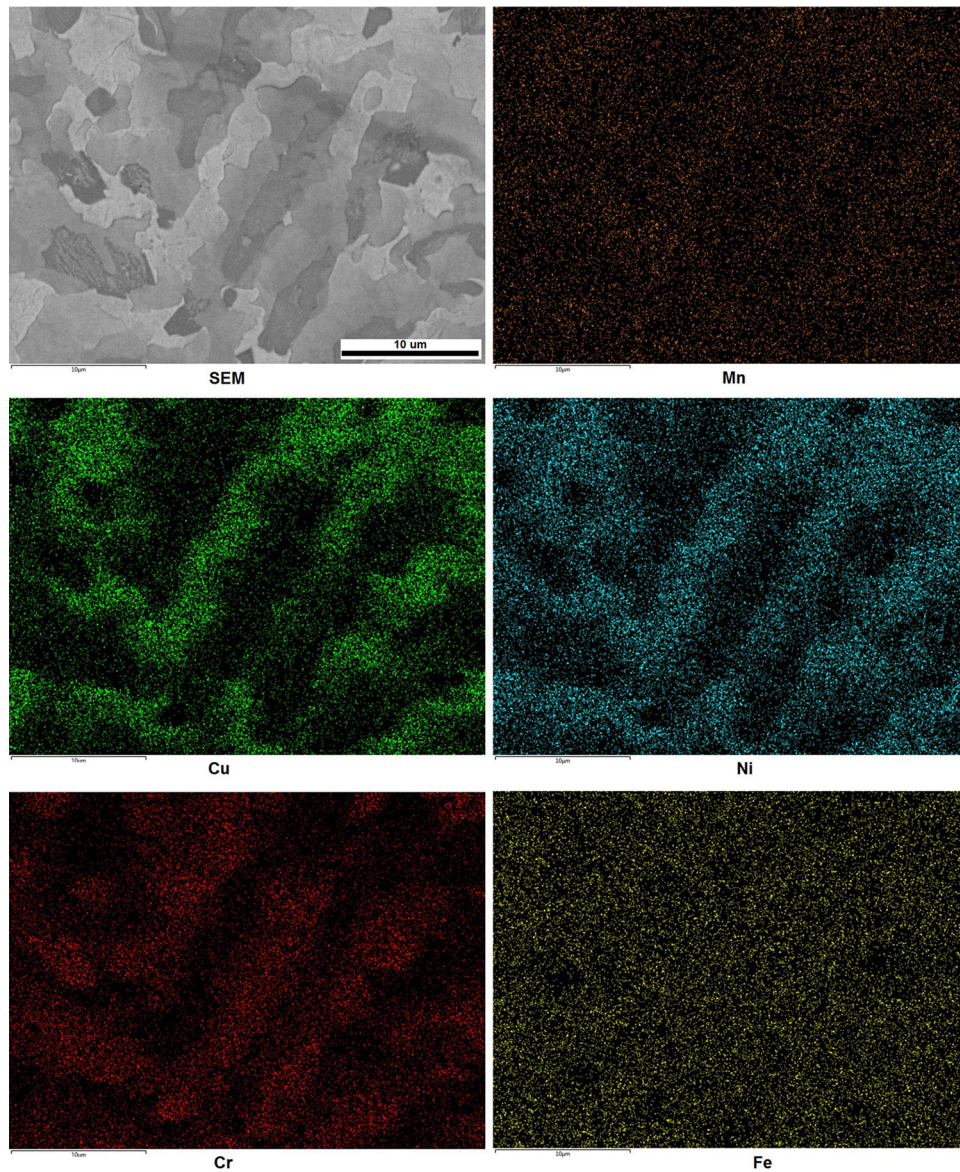


**Fig. 4** EDS maps of components for as-cast FeCrCuMnNi alloy

As previously noted, BCC-structured high-entropy alloys have high strength and low ductility, while FCC-structured alloys have lower strength but increased ductility (Ref 1). It is therefore expected that a combination of FCC and BCC phases leads to a good compromise between these two properties (Ref 1, 18). The presence of a continuous ductile matrix (FCC IDRs) in the alloy is the most important reason for the good ductility. On the other hand, the formation of the FCC2 phase with intermediate elemental distribution between FCC1 and BCC (Table 2) phases leads to a progressive transition between DRs and IDRs, which is likely to reduce stress concentration and crack nucleation during deformation, as compared with, for example, a two-phase composite.

Furthermore, in the high-entropy alloys, different atomic sizes, bonding energies and crystal structures among the constituent elements lead to high lattice distortions (Ref 1, 2). The hardness and strength of these alloys effectively increase due to these lattice distortions and their associated elastic stress field, which reduce dislocation mobility. Another way of

looking at the increased strength is to consider the large solution hardening effects.

Microhardness measurement promotes the above scenario, as 269, 310 and 391 HV were obtained for FCC1, FCC2 and BCC, respectively. The BCC phase was confirmed as the hardest phase, which is consistent with the general trend in HEAs (Ref 1, 2). The increased solution hardening effect, compared to FCC phases, might be due to difference in the coordination number (12 for FCC and 8 for BCC), which leads to a larger fraction of atomic pairs with unlike atoms (Ref 18). On the other hand, the difference in hardness of FCC phases might be due to a difference in the main elements, atomic radii, which is higher for FCC2 (Cr, Fe, Ni) than for FCC1 (Cu, Mn, Ni).

The measured strain hardening behavior can be rationalized using the simple Hollomon's equation (Ref 33, 34) (Eq 11) with a strain hardening exponent ( $n$ ) and the slope of  $\ln \varepsilon - \ln \sigma$  curve, expressed by Eq 12:

$$\sigma = K \varepsilon^n \quad (\text{Eq 11})$$

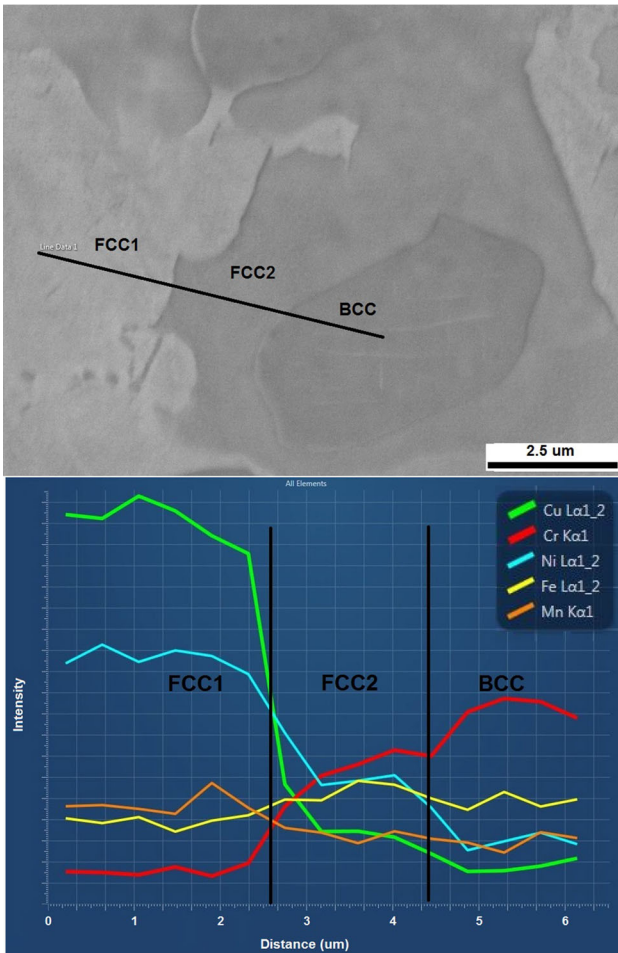


**Fig. 5** Line scan EDS result highlighting the composition of the three different phases

$$n = d(\ln \sigma) / d(\ln \varepsilon) \quad (\text{Eq 12})$$

In addition, the differential method of Crussard–Jaoul (C–J) can be used to study the strain hardening of the alloy. The following formula is derived by the differentiation of Eq 11.

$$\ln\left(\frac{d\sigma}{d\varepsilon}\right) = \ln(Kn) + (n - 1) \ln \varepsilon \quad (\text{Eq 13})$$

In the  $\ln \varepsilon - \ln(d\sigma/d\varepsilon)$  curve,  $(n - 1)$  is the slope of the curve. Modified (C–J) analysis is also presented by the Swift model, where the correlation between strain and stress is stated as follows (Ref 34):

$$\varepsilon = \varepsilon_0 + c\sigma^m \quad (\text{Eq 14})$$

where  $\varepsilon_0$  is the material constant,  $m$  is the reversed power of work hardening, and  $c$  is the material constant. The following formula is extracted by the differentiation of this equation:

$$\ln\left(\frac{d\sigma}{d\varepsilon}\right) = (1 - m) \ln \sigma - \ln cm \quad (\text{Eq 15})$$

In the  $\ln \sigma - \ln(d\sigma/d\varepsilon)$  curve,  $(1 - m)$  is the slope of the curve. Figure 8 reveals three different curves based on the three different analyses explained above. As shown in Fig. 8(a), the strain hardening behavior proceeded in two steps in Hollomon’s

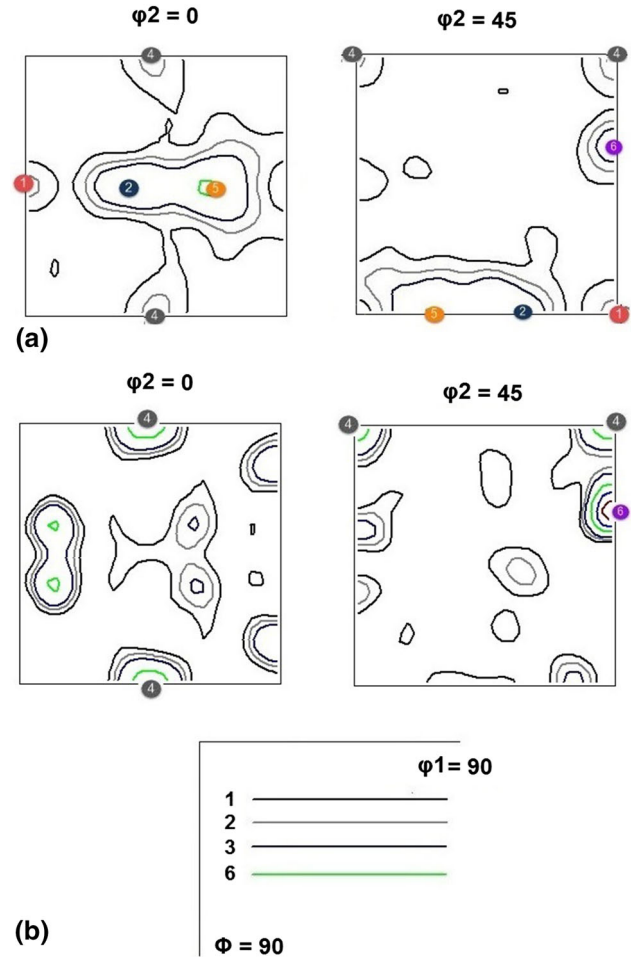


**Fig. 6**  $\varphi_2 = 0^\circ$  and  $45^\circ$  sections of ODF maps for the (a) FCC phase and (b) BCC phase

**Table 3** Important texture components studied in the FeCrCuMnNi alloy

Texture component	Miller indices	$\varphi_1$	$\Phi$	$\varphi_2$	Symbol
Goss	{110} <001>	0	45	0	①
Brass	{110} <112>	35	45	0	②
Rotated cube	{100} <011>	0	0	45	③
Goss/Brass (Twin)	{110} <111>	55	45	0	④
Copper	{112} <111>	90	35	45	⑤

method. The slope of the curve is smaller in the first step and increases with increasing strain which means that the alloy deforms with higher strain rate in the second step. In the first step, plastic deformation of the softer phase (FCC1) and elastic–plastic deformation of the harder phases occur, resulting in a low strain hardening rate. In this step, the FCC1 phases carry most of the deformation, while transferring load to the two other phases. In the second step, both FCC phases deform plastically, while the BCC phase deformation is elastic. The result is a more non-homogeneous deformation in the microstructure, and therefore an increased production of geometrically necessary dislocations, leading to an increased strain hardening rate compared to the first step (Ref 35–37). The

same process can be seen in the C–J and modified C–J methods as shown in Fig. 8(b) and (c), where the slopes are  $n - 1$  and  $1 - m$ , respectively. This behavior has also been reported in dual-phase steels, in which at the first stage with the low slope, the softer phase (ferrite matrix) deforms plastically, but the harder phase (martensite) remains elastic and, at the second stage with the high slope, both phases deform plastically (Ref 34, 35).

The fracture surface of the tensile test sample was studied using SEM and optical microscopy (OM) in order to evaluate the fracture mechanism (see Fig. 9). Ductile fracture with deep equiaxed dimples can be observed in this figure. Generally, ductile fracture occurs due to the formation and coalescence of microvoids ahead of the cracks. During plastic deformation, microvoids form in the alloy, mostly on the surfaces of phases, and then, join together. When the walls between these growing voids break, the final fracture occurs (Ref 38, 39). Excessive plastic deformation and the formation of a rough fracture surface with equiaxed, deep dimples are the characteristics of the fracture surfaces of the ductile metals. A high-magnification image confirms ductile fracture of the as-cast alloy, with such characteristic features, as shown in Fig. 9(b). Furthermore, Fig. 9(c) depicts the OM micrograph of the fracture surface from the transverse view. A rough fracture surface resulting from plastic deformation can be observed.

### 3.3 Heat Treatment

Figure 10 illustrates the XRD patterns of the heat-treated alloys at different temperatures. In this figure, as well as the as-cast sample two FCC phases and one BCC phase were observed in the heat-treated alloys. As can be seen, the structure of the alloy is stable after heat treatment up to 650 °C for 4 h. However, at temperatures of higher than 650 °C, two different phenomena take place. First, a  $\sigma$  phase of  $\text{Cr}_5\text{Fe}_6\text{Mn}_8$  composition forms after 4 h at 700 °C. This phase has a tetragonal structure with lattice constants  $a = 9.09 \text{ \AA}$  and  $c = 9.99 \text{ \AA}$  and results from the transformation of the BCC phase (Ref 40). Formation of binary or ternary intermetallic compounds during the annealing of HEAs has been reported in other systems (Ref 21, 40, 41). This compound reaches its maximum amount at 800 °C. However, it dissolves in the matrix at higher temperatures.

Second, the peaks of the BCC phase start decreasing in intensity with the increase in heat treatment temperature and reach their minimum intensity at 1000 °C. On the other hand,

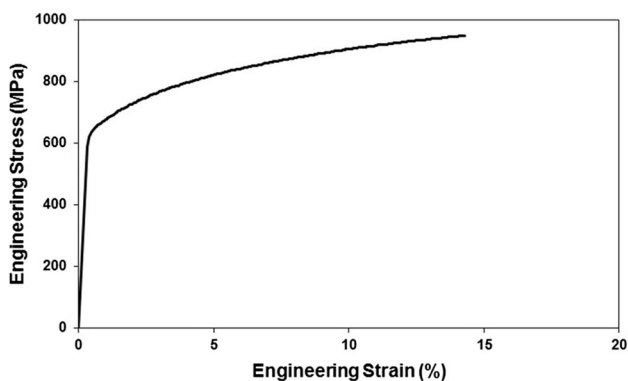
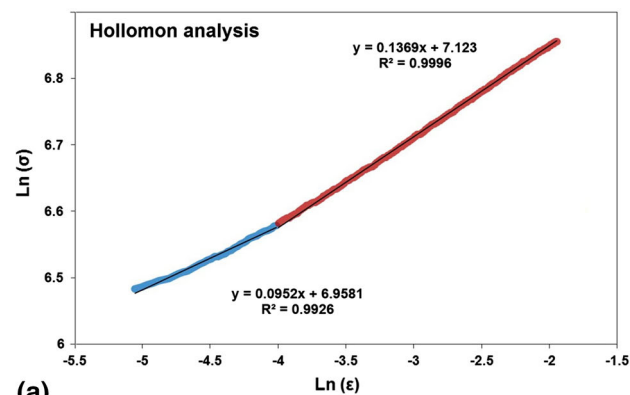


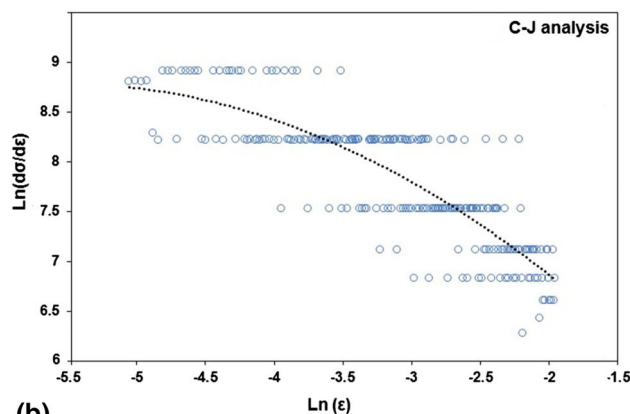
Fig. 7 Engineering stress–strain curve of FeCrCuMnNi high-entropy alloy under tension

Table 4 Tensile properties of different single-phase HEAs

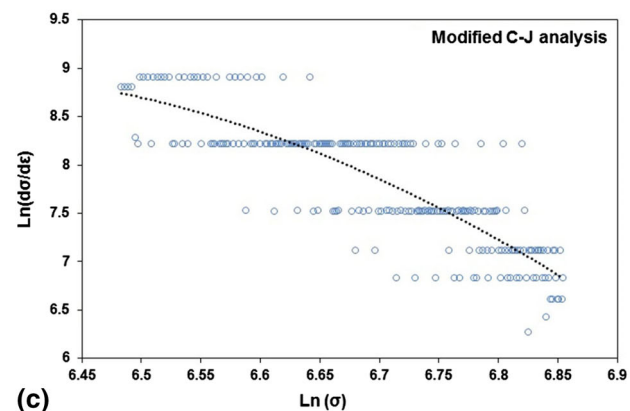
Alloy	Phase	UTS, MPa	Elongation, %	Ref
$\text{Al}_{0.3}\text{CoCrFeNi}$	FCC	350	55	(11)
$\text{FeCoCuNi}$	FCC	450	15	(30)
$\text{FeCoCuNiSn}_{0.2}$	FCC	250	3	(30)
$\text{AlCuCrFeNiCo}$	FCC	790	0.2	(13)
$\text{FeMnNiCuCo}$	FCC	450	14	(31)
$\text{FeCoNiCrMnAl}_{0.1}$	BCC	1150	4	(12)
$\text{TiZrNb}$	BCC	940	12	(32)



(a)



(b)



(c)

Fig. 8 Strain hardening behavior of the as-cast FeCrCuMnNi high-entropy alloy using (a) Hollomon’s method, (b) C–J method and (c) modified C–J method

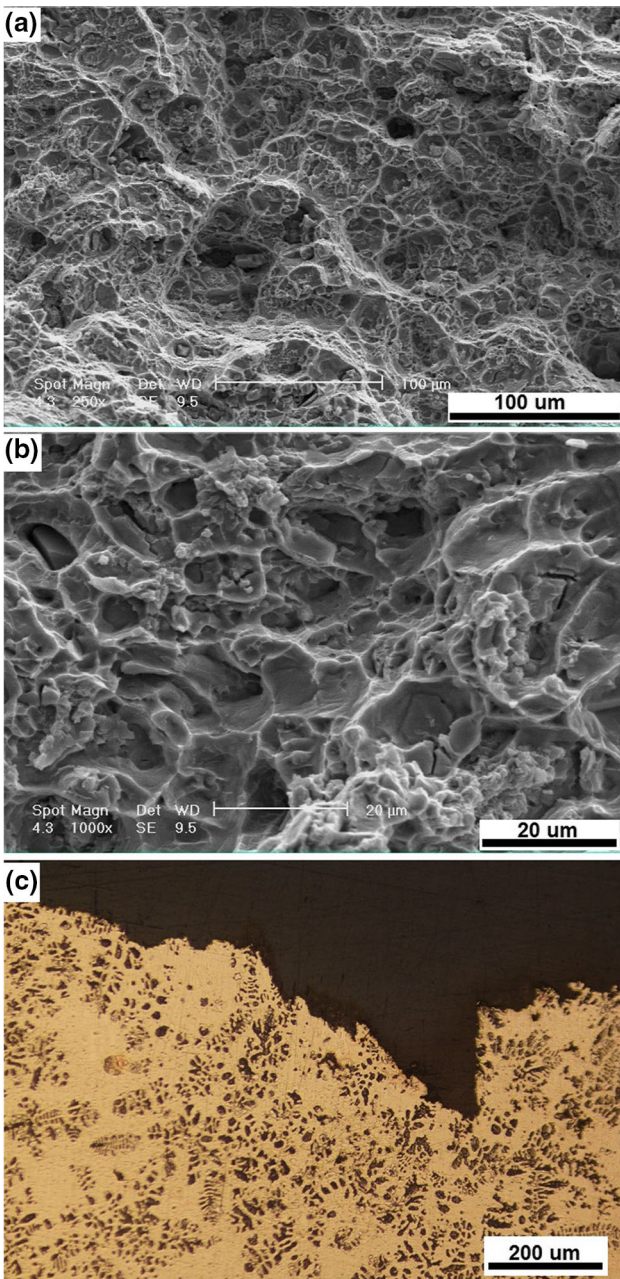


**Fig. 9** Fractographic features of the FeCrCuMnNi as-cast high-entropy alloy at the magnifications of (a) 250 × and (b) 1000 × and from (c) transverse view of fracture surface of the test specimen

peaks of the two FCC phases change in intensity during the different heat treatments. These variations in the XRD patterns can be directly related to the variations of the amounts of phases in the alloy.

The volume fractions of the  $\sigma$ , BCC and FCC phases can be roughly calculated using the following equation (Ref 17, 42):

$$W_p = \frac{P}{\sum P_i} \times 100\% \quad (\text{Eq 16})$$

where  $W_p$  is the volume fraction of the phase,  $P$  is the peak intensity of a given phase in the XRD pattern,  $i$  is the number of the phase, and  $\sum P_i$  is the total peak intensity of all phases in the XRD pattern. Variations of the volume fractions of the  $\sigma$ , FCC

and BCC phases during different annealing treatments are shown in Fig. 11. It is evident that, by increasing the annealing temperature, the FCC2 phase amount increases and reaches its maximum at 1000 °C. Inversely, the FCC1 and BCC amounts decrease with increasing temperature. About 20% and 72% reduction in the amount of FCC1 and BCC phases can be seen, respectively, when reaching the highest temperature. Furthermore,  $\sigma$  phase forms in the alloy structure from 700 °C and reaches its maximum amount at 800 °C; however, it almost dissolves entirely with the increase in heat treatment temperature.

Figure 12 presents the microstructures of the CrCuFeMnNi alloy after annealing at different temperatures. In addition, variations in the chemical composition of the three phases were measured using SEM-EDS analysis as shown in Table 5. Based on XRD and EDS results, BCC phase is rich in Cr and Fe and can be detected as DRs (see Fig. 12a). The gray regions around the dendrites (FCC2 phase) are rich in Fe and Ni, and the matrix of the alloy (IDRs) (FCC1 phase) shows Cu enrichment. The dendritic structure of the alloy is almost stable after heat treatment at temperatures of up to 800 °C (Fig. 12a–c). However, the alloy structure entirely changes when reaching 1000 °C. Figure 12(c) shows that at 800 °C, the growth of the FCC2 phase and dissolution of the BCC phase accelerate. As shown in Fig. 2, between 700 and 800 °C about 20% of the BCC phase dissolves, while the FCC2 amount increases by almost 15%, with respect to the as-cast sample. At this temperature, the FCC2 phase starts growing around the DRs (BCC phase). After annealing at 1000 °C, the dendritic structure disappears; DRs dissolve into the alloy matrix, and the FCC2 phase spheroidizes. These findings of the microstructural observation are completely consistent with the XRD results (see Fig. 10).

In HEAs, the random substitution among the elements can increase the lattice distortion energy due to the variable atomic radii, which then leads to the formation of metastable phases under non-equilibrium conditions. The phase distribution changes to reduce lattice distortion when the supersaturated solid solution is annealed at a high temperature (Ref 43). In addition, according to the expression of the Gibbs free energy, the following is true (Ref 1):

$$G_{\text{mix}} = H_{\text{mix}} - TS_{\text{mix}} \quad (\text{Eq 17})$$

The free energy decreases due to high entropy of mixing which leads to the stabilization of the phases. The entropy of mixing can be estimated in a solid solution using Boltzmann's equation (Ref 1, 22):

$$\Delta S_{\text{conf}} = -k \ln w = -R \sum x_i \ln x_i \quad (\text{Eq 18})$$

where  $\Delta S_{\text{conf}}$  is the entropy of mixing,  $k$  is the Boltzmann constant,  $w$  is the number of mixed states,  $x_i$  is the mole percent of  $i$  component, and  $R$  is the gas constant. The amount of entropy of mixing for the BCC, FCC1 and FCC2 phases of the as-cast alloy, evaluated using Eq 18 and the data reported in Table 5, is 11.6, 11.1 and 12.8 J/K mol<sup>-1</sup>, respectively. It is clear that the FCC2 phase has the maximum amount of entropy; hence, it has a stability advantage. This is consistent with the growth of the FCC2 phase during annealing at high temperatures. Transformation of the BCC phase to FCC has also been observed in annealing processes of other HEA systems (Ref 25, 41, 43).



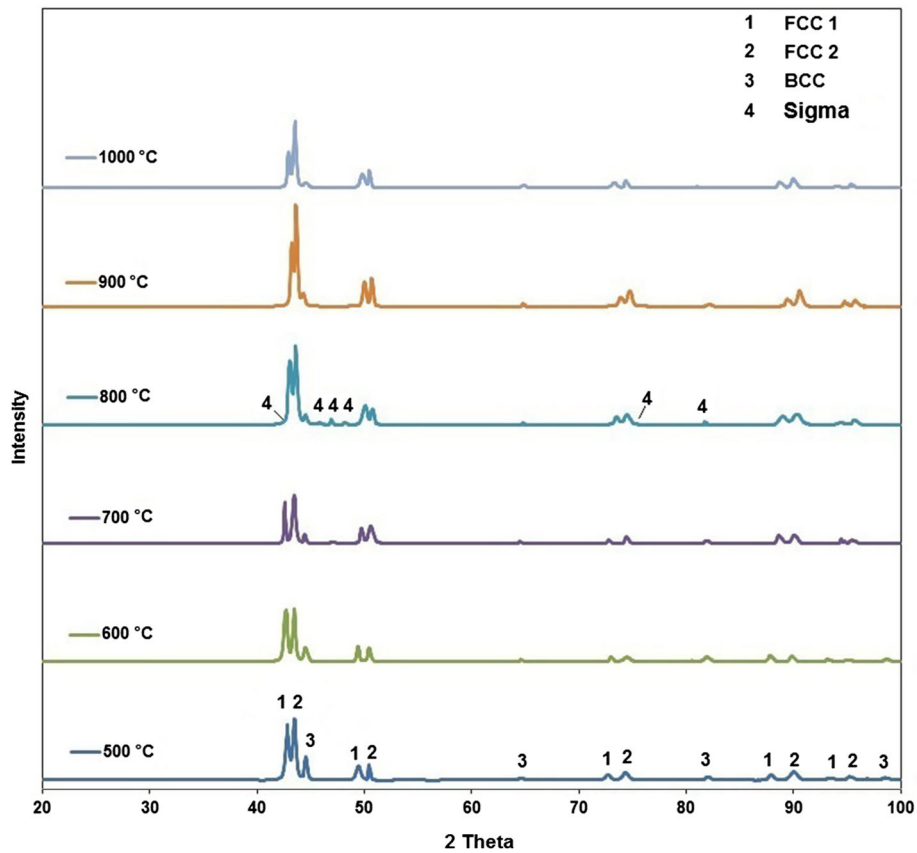


Fig. 10 XRD patterns of the CrCuFeMnNi alloy after heat treatment at different temperature

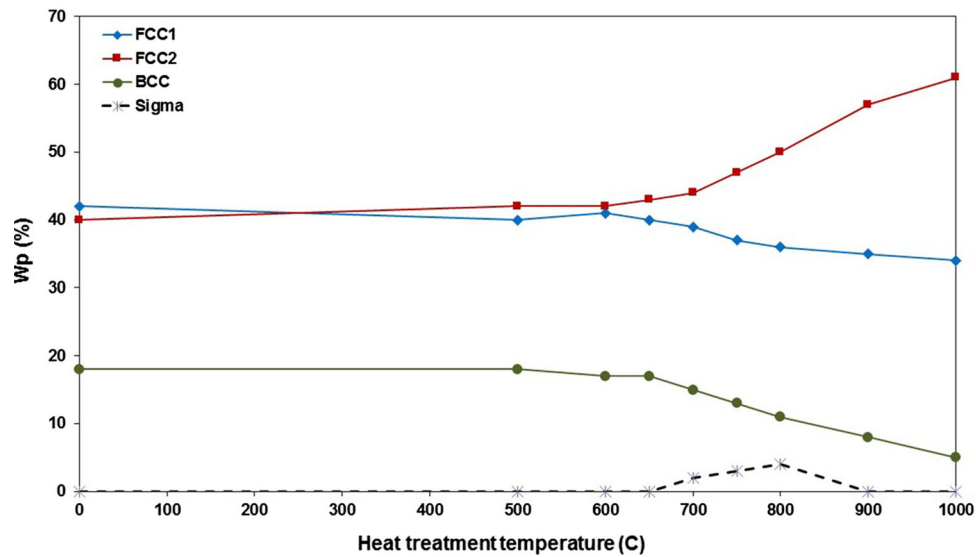
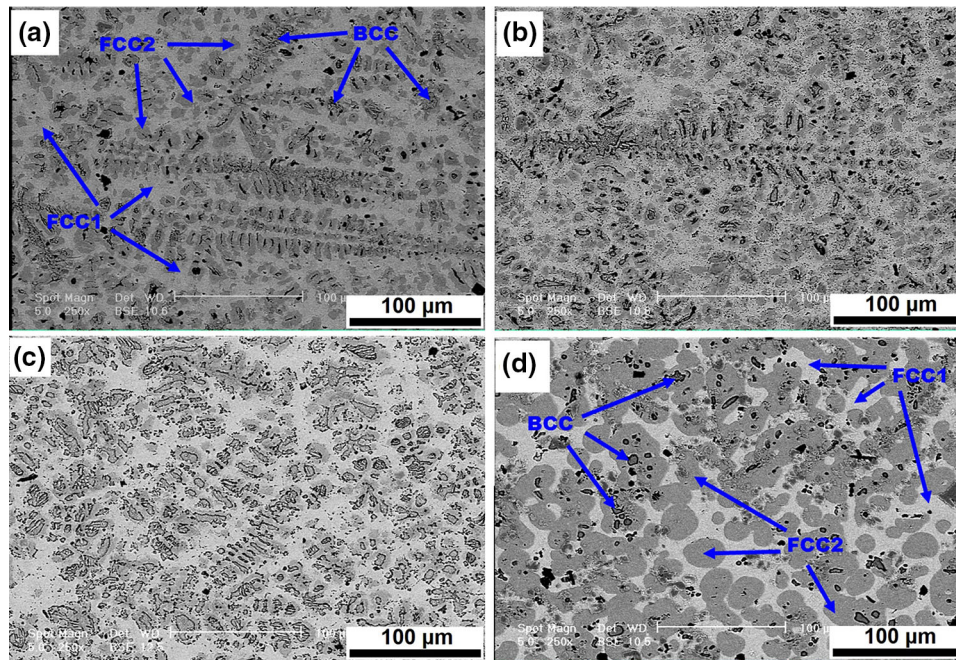


Fig. 11 Variations of the volume fraction of  $\sigma$ , FCC and BCC phases by heat treatment temperature

Table 5 shows that chemical compositions clearly vary with the annealing treatment. As revealed in Fig. 12(d), after 4 h of annealing at the temperature of 1000 C, only small parts of the BCC phase remain (about 5 vol.% in Fig. 11). These small parts are mainly saturated with Cr (~ 50%) and Fe (~ 35%). Moreover, some regions of the FCC1 phase transform into FCC2 phase, and the remaining parts are enriched with Cu.

Consequently, the FCC1 phase regions contain mainly Cu (~ 55%), Mn (~ 20%) and Ni (~ 17%). Furthermore, the FCC2 phase which grows and becomes the major phase approximately retains its composition. This phase includes mainly Fe (~ 35%), Ni (27%) and Cr (~ 25%). In fact, the FCC2 phase grows by the absorption of atoms from neighboring phases, which leads to the shrinking of these phases and



**Fig. 12** SEM micrographs of the heat-treated alloys at temperatures of (a) 500 °C, (b) 700 °C, (c) 800 °C and (d) 1000 °C

**Table 5** Chemical compositions (at.%) of three phases of the FeCrCuMnNi alloy after different heat treatment temperatures

Structure	Fe	Cr	Cu	Mn	Ni
500 °C					
BCC	33.5	42.3	3.1	10.8	10.3
FCC1	6.4	3.1	46.3	24.0	20.2
FCC2	27.3	24.0	7.1	14.9	26.7
700 °C					
BCC	33.7	44.4	2.5	8.8	10.7
FCC1	7.1	2.9	46.5	23.5	20.0
FCC2	32.8	23.4	4.8	12.9	26.1
800 °C					
BCC	33.4	46.9	2.1	8.1	9.5
FCC1	6.7	2.8	48.9	22.1	19.5
FCC2	33.5	24.5	4.0	11.3	26.7
1000 °C					
BCC	34.7	49.3	1.2	6.1	8.7
FCC1	6.5	3.0	53.7	19.6	17.2
FCC2	34.7	25.0	4.1	8.9	27.3

their enrichment in some elements (FCC1 in Cu and BCC in Cr).

#### 4. Conclusion

A FeCrCuMnNi high-entropy alloy was produced with a mixture of two FCC phases and one BCC phase. The microstructure and mechanical properties of the as-cast sample were investigated using different tests. The following conclusions could be drawn from this research:

1. Thermodynamic analysis illustrates the solid solution formation, and based on microstructural observations, the al-

- loy can be divided into three regions: the BCC phase (DRs) which is saturated in Cr and Fe elements, FCC1 phase (IDRs) enriched in Cu and Ni and FCC2 phase (IDRs) which is rich in Fe, Ni and Cr.
2. EBSD results revealed that G/B(T) and Brass are the major texture components in the FCC phases and Rt-C and Copper components form in BCC phase. In addition, it was seen that the as-cast alloy includes almost 18 vol.% of BCC phase and 82% of the FCC phases.
3. The combination of FCC and BCC phases with different characteristics led to an excellent compromise between strength and ductility, and the alloy revealed a tensile strength of ~ 950 MPa, yield strength of ~ 615 MPa and elongation of 14%.
4. Dual strain hardening behavior of the alloy revealed the enhancement of hardening coefficient by increasing deformation in different analyses which were the same as the behavior of dual-phase steels.
5. The as-cast alloy fractographs showed a typical ductile fracture with equiaxed, deep dimples.
6. Phase composition of the alloy remained stable during annealing up to 650 °C. Between 650 and 850 °C, a  $\sigma$  phase formed. However, this phase and the DRs (BCC phase) almost dissolved in the matrix at 1000 °C. After such a treatment, the alloy structure mostly consisted of spherical FCC2 phase in the FCC1 matrix. The growth of the FCC2 phase is related to higher entropy contribution compared to the other phases.

#### References

1. Y. Zhang, T.T. Zuo, Z. Tang, M.C. Gao, K.A. Dahmen, P.K. Liaw, and Z.P. Lu, Microstructures and Properties of High-Entropy Alloys, *Prog. Mater. Sci.*, 2014, **61**, p 1–93

2. C. Li, Y. Xue, M. Hua, T. Cao, L. Ma, and L. Wang, Microstructure and Mechanical Properties of  $\text{Al}_x\text{Si}_{0.2}\text{CrFeCoNiCu}_{1-x}$  High-Entropy Alloys, *Mater. Des.*, 2016, **90**, p 601–609
3. S. Zhao, Y. Shao, X. Liu, N. Chen, H. Ding, and K. Yao, Pseudo-Quinary  $\text{Ti}_{20}\text{Zr}_{20}\text{Hf}_{20}\text{Be}_{20}$  ( $\text{Cu}_{20-x}\text{Ni}_x$ ) High Entropy Bulk Metallic Glasses with Large Glass Forming Ability, *Mater. Des.*, 2015, **87**, p 625–631
4. J.W. Yeh, S.K. Chen, S.J. Lin, J.Y. Gan, T.S. Chin, T.T. Shun, C.H. Tsau, and S.Y. Chang, Nanostructured High-Entropy Alloys with Multiple Principal Elements: Novel Alloy Design Concepts and Outcomes, *Adv. Eng. Mater.*, 2004, **6**(5), p 299–303
5. T.S. Reddy, I.S. Wani, T. Bhattacharjee, S.R. Reddy, R. Saha, and P.P. Bhattacharjee, Severe Plastic Deformation Driven Nanostructure and Phase Evolution in a  $\text{Al}_{0.5}\text{CoCrFeMnNi}$  Dual Phase High Entropy Alloy, *Intermetallics*, 2017, **91**, p 150–157
6. D.G. Shaysultanov, G.A. Salishchev, Y.V. Ivanisenko, S.V. Zherebtsov, M.A. Tikhonovsky, and N.D. Stepanov, Novel  $\text{Fe}_{36}\text{Mn}_{21}\text{Cr}_{18}\text{Ni}_{15}\text{Al}_{10}$  High Entropy Alloy with bcc/B2 Dual-Phase Structure, *J. Alloys Compd.*, 2017, **705**, p 756–763
7. Z. Li and D. Raabe, Influence of Compositional Inhomogeneity on Mechanical Behavior of an Interstitial Dual-Phase High-Entropy Alloy, *Mater. Chem. Phys.*, 2017, **210**, p 29–36
8. A. Shabani, M.R. Toroghinejad, A. Shafeyi, and P. Cavaliere, Effect of Cold-Rolling on Microstructure, Texture and Mechanical Properties of an Equiatomic  $\text{FeCrCuMnNi}$  High Entropy Alloy, *Materialia*, 2018, **1**, p 175–184
9. A. Shabani, M.R. Toroghinejad, A. Shafeyi, and R.E. Logé, Evaluation of the Mechanical Properties of the Heat Treated  $\text{FeCrCuMnNi}$  High Entropy Alloy, *Mater. Chem. Phys.*, 2019, **221**, p 68–77
10. Y. Wu, Y. Cai, T. Wang, J. Si, J. Zhu, Y. Wang, and X. Hui, A Refractory  $\text{Hf}_{25}\text{Nb}_{25}\text{Ti}_{25}\text{Zr}_{25}$  High-Entropy Alloy with Excellent Structural Stability and Tensile Properties, *Mater. Lett.*, 2014, **130**, p 277–280
11. T.-T. Shun and Y.-C. Du, Microstructure and Tensile Behaviors of FCC  $\text{Al}_{0.3}\text{CoCrFeNi}$  High Entropy Alloy, *J. Alloys Compd.*, 2009, **479**(1), p 157–160
12. J. He, W. Liu, H. Wang, Y. Wu, X. Liu, T. Nieh, and Z. Lu, Effects of Al Addition on Structural Evolution and Tensile Properties of the  $\text{FeCoNiCrMn}$  High-Entropy Alloy System, *Acta Mater.*, 2014, **62**, p 105–113
13. A. Kuznetsov, D. Shaysultanov, N. Stepanov, G. Salishchev, and O. Senkov, Tensile Properties of an  $\text{AlCrCuNiFeCo}$  High-Entropy Alloy in As-Cast and Wrought Conditions, *Mater. Sci. Eng. A*, 2012, **533**, p 107–118
14. Y. Lu, Y. Dong, S. Guo, L. Jiang, H. Kang, T. Wang, B. Wen, Z. Wang, J. Jie, and Z. Cao, A Promising New Class of High-Temperature Alloys: Eutectic High-Entropy Alloys, *Sci. Rep.*, 2014, **4**, p 6200
15. B. Ren, Z. Liu, D. Li, L. Shi, B. Cai, and M. Wang, Effect of Elemental Interaction on Microstructure of  $\text{CuCrFeNiMn}$  High Entropy Alloy System, *J. Alloys Compd.*, 2010, **493**(1), p 148–153
16. C. Li, J. Li, M. Zhao, and Q. Jiang, Effect of Alloying Elements on Microstructure and Properties of Multiprincipal Elements High-Entropy Alloys, *J. Alloys Compd.*, 2009, **475**(1), p 752–757
17. B. Ren, Z. Liu, B. Cai, M. Wang, and L. Shi, Aging Behavior of a  $\text{CuCr}_2\text{Fe}_2\text{NiMn}$  High-Entropy Alloy, *Mater. Des.*, 2012, **33**, p 121–126
18. B. Murty, J.-W. Yeh, and S. Ranganathan, *High-Entropy Alloys*, Butterworth-Heinemann, London, 2014
19. X. Yang and Y. Zhang, Prediction of High-Entropy Stabilized Solid-Solution in Multi-Component Alloys, *Mater. Chem. Phys.*, 2012, **132**(2), p 233–238
20. A. Takeuchi and A. Inoue, Calculations of Mixing Enthalpy and Mismatch Entropy for Ternary Amorphous Alloys, *Mater. Trans. JIM*, 2000, **41**(11), p 1372–1378
21. K. Zhang and Z. Fu, Effects of Annealing Treatment on Phase Composition and Microstructure of  $\text{CoCrFeNiTiAl}_x$  High-Entropy Alloys, *Intermetallics*, 2012, **22**, p 24–32
22. O. Senkov and D. Miracle, A New Thermodynamic Parameter to Predict Formation of Solid Solution or Intermetallic Phases in High Entropy Alloys, *J. Alloys Compd.*, 2016, **658**, p 603–607
23. U. Hsu, U. Hung, J. Yeh, S. Chen, Y. Huang, and C. Yang, Alloying Behavior of Iron, Gold and Silver in  $\text{AlCoCrCuNi}$ -Based Equimolar High-Entropy Alloys, *Mater. Sci. Eng. A*, 2007, **460**, p 403–408
24. N. Nayan, G. Singh, S. Murty, A.K. Jha, B. Pant, K.M. George, and U. Ramamurty, Hot Deformation Behaviour and Microstructure Control in  $\text{AlCrCuNiFeCo}$  High Entropy Alloy, *Intermetallics*, 2014, **55**, p 145–153
25. Y. Zhuang, H. Xue, Z. Chen, Z. Hu, and J. He, Effect of Annealing Treatment on Microstructures and Mechanical Properties of  $\text{FeCoNiCuAl}$  High Entropy Alloys, *Mater. Sci. Eng. A*, 2013, **572**, p 30–35
26. G.D. Sathiaraj, P.P. Bhattacharjee, C.-W. Tsai, and J.-W. Yeh, Effect of Heavy Cryo-Rolling on the Evolution of Microstructure and Texture During Annealing of Equiatomic  $\text{CoCrFeMnNi}$  High Entropy Alloy, *Intermetallics*, 2016, **69**, p 1–9
27. P. Bhattacharjee, G. Sathiaraj, M. Zaid, J. Gatti, C. Lee, C.-W. Tsai, and J.-W. Yeh, Microstructure and Texture Evolution During Annealing of Equiatomic  $\text{CoCrFeMnNi}$  High-Entropy Alloy, *J. Alloys Compd.*, 2014, **587**, p 544–552
28. G.D. Sathiaraj and P.P. Bhattacharjee, Analysis of Microstructure and Microtexture During Grain Growth in Low Stacking Fault Energy Equiatomic  $\text{CoCrFeMnNi}$  High Entropy and Ni–60 wt.% Co Alloys, *J. Alloys Compd.*, 2015, **637**, p 267–276
29. I.S. Wani, T. Bhattacharjee, S. Sheikh, I.T. Clark, M.H. Park, T. Okawa, S. Guo, P.P. Bhattacharjee, and N. Tsuji, Cold-Rolling and Recrystallization Textures of a Nano-Lamellar  $\text{AlCoCrFeNi}_{2.1}$  Eutectic High Entropy Alloy, *Intermetallics*, 2017, **84**(Supplement C), p 42–51
30. L. Liu, J. Zhu, C. Zhang, J. Li, and Q. Jiang, Microstructure and the Properties of  $\text{FeCoCuNiSn}_x$  High Entropy Alloys, *Mater. Sci. Eng. A*, 2012, **548**, p 64–68
31. L. Liu, J. Zhu, L. Li, J. Li, and Q. Jiang, Microstructure and Tensile Properties of  $\text{FeMnNiCuCoSn}_x$  High Entropy Alloys, *Mater. Des.*, 2013, **44**, p 223–227
32. Y. Zhang and W. Jie Peng, Microstructural Control and Properties Optimization of High-Entropy Alloys, *Proc. Eng.*, 2012, **27**, p 1169–1178
33. J.H. Hollomon, Tensile Deformation, *AIME Trans.*, 1945, **12**(4), p 1–22
34. Y.I. Son, Y.K. Lee, K.-T. Park, C.S. Lee, and D.H. Shin, Ultrafine Grained Ferrite–Martensite Dual Phase Steels Fabricated Via Equal Channel Angular Pressing: Microstructure and Tensile Properties, *Acta Mater.*, 2005, **53**(11), p 3125–3134
35. N. Saedi, M. Karimi, and M. Toroghinejad, Development of a New Dual Phase Steel with Laminated Microstructural Morphology, *Mater. Chem. Phys.*, 2017, **192**, p 1–7
36. F.J. Humphreys and M. Hatherly, *Recrystallization and Related Annealing Phenomena*, 2nd ed., Elsevier, Amsterdam, 2004
37. P. Cavaliere, B. Sadeghi, and A. Shabani, Carbon Nanotube Reinforced Aluminum Matrix Composites Produced by Spark Plasma Sintering, *J. Mater. Sci.*, 2017, **52**(14), p 8618–8629
38. A. Shabani and M.R. Toroghinejad, Investigation of the Microstructure and the Mechanical Properties of Cu–NiC Composite Produced by Accumulative Roll Bonding and Coating Processes, *J. Mater. Eng. Perform.*, 2015, **24**(12), p 4746–4754
39. A. Shabani and M.R. Toroghinejad, Study on Texture Evolution and Shear Behavior of an  $\text{Al/Ni/Cu}$  Composite, *J. Mater. Eng. Perform.*, 2018, **27**(11), p 6004–6015
40. S.T. Chen, W.Y. Tang, Y.F. Kuo, S.Y. Chen, C.H. Tsau, T.T. Shun, and J.W. Yeh, Microstructure and Properties of Age-Hardenable  $\text{Al}_x\text{CrFe}_{1.5}\text{MnNi}_{0.5}$  Alloys, *Mater. Sci. Eng. A*, 2010, **527**(21), p 5818–5825
41. L. Tsao, C. Chen, and C. Chu, Age Hardening Reaction of the  $\text{Al}_{0.3}\text{CrFe}_{1.5}\text{MnNi}_{0.5}$  High Entropy Alloy, *Mater. Des.*, 2012, **36**, p 854–858
42. R.E. Reed-Hill and R. Abbaschian, *Physical Metallurgy Principles*, Brooks/Cole Engineering Division Monterey, Monterey, 1973
43. K. Zhang, Z. Fu, J. Zhang, J. Shi, W. Wang, H. Wang, Y. Wang, and Q. Zhang, Annealing on the Structure and Properties Evolution of the  $\text{CoCrFeNiCuAl}$  High-Entropy Alloy, *J. Alloys Compd.*, 2010, **502**(2), p 295–299

**Publisher's Note** Springer Nature remains neutral with regard to jurisdictional claims in published maps and institutional affiliations.